Persistent Scatterer Analysis Using Dual-Polarization Sentinel-1 Data: Contribution From VH Channel

Roghayeh Shamshiri, Hossein Nahavandchi, and Mahdi Motagh

***Abstract*—The regular acquisition and relatively short revisit time of Sentinel-1 satellite improve the capability of a persistent scatterer interferometric synthetic aperture radar (PS-InSAR) as a suitable geodetic method of choice for measuring ground surface deformation in space and time. The SAR instrument aboard the Sentinel-1 satellite supports operation in dual polarization (HH–HV, VV–VH), which can be used to increase the spatial density of measurement points through the polarimetric optimization method. This study evaluates the improvement in displacement mapping by incorporating the information obtained from the VH channel of Sentinel-1 data into the PS-InSAR analysis. The method that has shown great success with different polarimetric data performs a search over the available polarimetric space in order to find a linear combination of polarization states, which yields the optimum PS selection criterion using the amplitude dispersion index (ADI) criterion. We applied the method to a dataset of 50 dual-polarized (VV–VH) Sentinel-1 images over Trondheim city in Norway. The results show overall increase of about 186% and 78% in the number of PS points with respect to the conventional channels of VH and VV, respectively. The study concludes that, using the ADI optimization, we can incorporate information from the VH channel into the PS-InSAR analysis, which otherwise is lost due to its low amplitude.**

***Index Terms*—Dual polarization, optimization, persistent scatterer interferometric synthetic aperture radar (PS-InSAR), sentinel-1.**

I. Introduction

PERSISTENT scatterer interferometric synthetic aperture radar (PS-InSAR) has proved to be a powerful geodetic technique to measure deformations of the earth's surface in space and time using a stack of synthetic aperture radar (SAR) images [1]–[7]. It has been widely used by the scientific community to measure the displacement related to subsidence/uplift [8], [9], landslide [10], [11], tectonic [12]–[14], and volcanoes [5], [15]. In order to minimize spatiotemporal decorrelation effects and other sources of errors, the PS-InSAR technique processes only those pixels, known as persistent scatterer (PS), that their decorrelation effects are negligible under certain quality criterion. The most commonly used criteria in the PS-InSAR method are coherence stability [7], [16] and the amplitude dispersion index (ADI) [4].

Traditionally, the PS-InSAR method has been formulated and applied to single-polarimetric SAR data because of the limitations of available multipolarimetric SAR images. However, the recent launch of new satellites with capability of multipolarimetric acquisition motivated researchers to develop new techniques based on the polarimetric optimization. The approach has been applied to optimize the coherence in differential InSAR (DInSAR) [17], [18]. Coherence optimization algorithms have been evaluated for copolar (HH–VV) and cross-polar channels (HH–HV), in addition to the quad-polarized ALOS data for the DInSAR analysis [19].

It has also been applied on a multibaseline InSAR [20]. In the context of multibaseline, a search over the available polarimetric space is performed to find a channel that optimizes the phase-stability criteria, which in turn increases the number of measurement points and consequently enhances the performance of the method. The approach has been implemented on the PS-InSAR method by optimizing the coherence stability and the ADI [21]–[24]. Navarro-Sanchez *et al.* implemented the polarimetric optimization for the ADI for copolar and cross-polar channels in addition to the quad-polarized RADARSAT-2 data for the PS-InSAR analysis [25]. The PS selection procedure has also been optimized using signal-to-noise ratio [26], the temporal sublook coherence [27], [28] criteria with dual/multipolarized data, maximum likelihood function [29], and phase-difference between copolarized components [30]. The efficiency of the approach has also been proved in the small baseline method [31], [32].

The recent launch of the Sentinel-1 mission with capability to obtain acquisitions on dual-polarized (HH–HV, VV–VH) channels can help improving PS-InSAR analyses by increasing the PS density. In general, having more than one polarimetric channel helps to increase the PS density, especially in urban areas [21]–[23], [33], in which each resolution cell has a single dominant scattering mechanism. However, the amplitude of the cross-polar measurements is generally smaller than that of the copolar channels. Therefore, they may suffer more degradation due to noise, and their information might be lost in a single-polarized time-series analysis. Using the optimization method, we can incorporate their information into displacement mapping.

Manuscript received September 4, 2017; revised January 10, 2018 and April 30, 2018; accepted May 31, 2018. This work was supported by the Norwegian University of Science and Technology. *(Corresponding author: Roghayeh Shamshiri.)*

R. Shamshiri and H. Nahavandchi are with the Department of Civil and Environmental Engineering, Norwegian University of Science and Technology, Trondheim 7491, Norway (e-mail: roghayeh.shamshiri@ntnu.no; hossein.nahavandchi@ntnu.no).

M. Motagh is with GFZ German Research Center for Geosciences, Potsdam 14473, Germany, and also with Leibniz University, Hannover 30167, Germany (e-mail: motagh@gfz-potsdam.de).

Color versions of one or more of the figures in this paper are available online at http://ieeexplore.ieee.org.

Digital Object Identifier 10.1109/JSTARS.2018.2848111

In this study, we exploit the polarimetric information available in Sentinel-1 data (VV–VH) to investigate how the contribution of the VH channel affects the improvement of the PS-InSAR method over urban areas. We apply the approach presented in the previously published paper [21], but utilized it for Sentinel-1, due to easy access to the dataset and its free availability. Our goal is to analyze the performance of the approach. Trondheim city, located in central Norway, has been chosen as a test area. The city consists of several types of targets, which help to investigate the PS density and the phase-quality variations better as a function of the target types. These have been focused particularly in this study.

II. Method

A. StaMPS

The PS-InSAR method implemented in StaMPS works based on the spatial correlation approach. First, for computational reasons, an initial set of PS candidates (PSCs) is identified based on the ADI, defined as the ratio between standard deviation (σ_a) and mean ($\bar{a}$) of the amplitudes [4]

$$D_A = \frac{\sigma_a}{\bar{a}} = \frac{\sqrt{\sum_{i=1}^{N}\left(|s_i| - \overline{|s|}\right)^2 / N}}{\sum_{i=1}^{N}|s_i| / N} \quad (1)$$

where s is a complex value of a single-look complex (SLC) pixel, $|s_i|$ is the amplitude of the pixel in the ith SLC, and N is the number of SLCs. The lower the ADI values, the higher the phase quality. Therefore, pixels with the ADI less than a predefined threshold are selected as PSC points.

In the next step, for each PSC in each differential interferograms ($\psi_{x,i}$), the spatially correlated terms ($\tilde{\psi}_{x,i}$) including deformation, atmospheric signal, orbital inaccuracies, and spatially correlated part of the topographic phase due to the digital elevation model (DEM) errors, are estimated using a combination of low-pass and adaptive (Goldstein) phase filters iteratively [34]. The spatially uncorrelated part of the topographic phase ($\Delta\hat{\psi}^{u}_{\theta,x,i}$), which is correlated with the perpendicular baseline, is estimated by least-squares inversion. The temporal coherence (γ_x) is then calculated from residuals as follows [35]:

$$\gamma_x = \frac{1}{N}\left|\sum_{i=1}^{N} \exp\left\{j\left(\psi_{x,i} - \tilde{\psi}_{x,i} - \Delta\hat{\psi}^{u}_{\theta,x,i}\right)\right\}\right|. \quad (2)$$

Contribution of each pixel is weighted based on its estimated temporal coherence, followed by the re-estimation of the DEM error and the temporal coherence. This algorithm is iterated several times until the root-mean-square change in the temporal coherence ceases to decrease. Then, pixels are selected as PS points, considering their amplitude dispersion as well as their final temporal coherence. Afterward, three-dimensional phase unwrapping is done on the PS points [36]. The unwrapped phase of PS points is filtered using high-pass filtering in time and a low-pass filtering in space to estimate the atmospheric and orbital errors. Subtracting these terms from the unwrapped phase of each PS leaves the ground deformation estimate. Further details regarding StaMPS can be found in the relevant literatures [5], [35].

B. Polarimetric SAR

A fully polarimetric SAR measures a complex scattering matrix S at each pixel, which describes the scattering process of a target

$$S = \begin{bmatrix} S_{\mathrm{hh}} & S_{\mathrm{vh}} \\ S_{\mathrm{vh}} & S_{\mathrm{vv}} \end{bmatrix}. \quad (3)$$

Using the Pauli basis [37], the corresponding scattering vector $\underline{K}$ can be derived for each resolution element as follows:

$$\underline{K} = \frac{1}{\sqrt{2}}\left[\, S_{\mathrm{hh}} + S_{\mathrm{vv}} \;\; S_{\mathrm{hh}} - S_{\mathrm{vv}} \;\; 2S_{\mathrm{vh}} \,\right]^T \quad (4)$$

where T is the transpose operator, and S_{hh}, S_{vv}, and S_{vh} are the elements of matrix S standing for the copolar channels and the cross-polar channel. By defining a unitary complex projection vector $\underline{\omega}$, it is possible to generate a complex scalar image by projecting the scattering vector of each pixel, i onto μ, as

$$\mu_i = \omega_i^H \underline{K}_i \quad (5)$$

where H denotes conjugate transpose operation.

Equation (5) suggests that the optimization can be performed by choosing suitable polarimetric states $\underline{\omega}$ for each pixel. There are two general approaches for the polarimetric optimization of multibaseline interferograms. These are multibaseline equal scattering mechanism (MB-ESM) and multibaseline multiple scattering mechanism (MB-MSM) [20]. An important point to note is that as the polarimetric properties of the scene are not changed between data acquisitions, a single polarimetric state, i.e., ESM, is used for all acquisitions [20].

C. Modification of the Formulas for Dual-Polarized Sentinel-1 Data

The formulations stated in Section II-B are proposed for the fully polarimetric SAR. In this section, they are modified to be used for analyzing the dual-polarized SAR images of Sentinel-1. The scattering matrix and the corresponding scattering vector of VH–VV are, respectively, (see, e.g., [38], eqs. (18) and (19)], [39], eq. (3)),

$$S = \begin{bmatrix} 0 & S_{\mathrm{vh}} \\ S_{\mathrm{vh}} & S_{\mathrm{vv}} \end{bmatrix} \quad (6)$$

and

$$\underline{K} = \frac{1}{\sqrt{2}}\left[\, S_{\mathrm{vv}} \;\; 2S_{\mathrm{vh}} \,\right]^T. \quad (7)$$

Following the method developed by Cloude and Papathanasiou [37], in which the polarimetric state $\underline{\omega}$ is derived as eigenvectors for coherence optimization, the reduced version of $\underline{\omega}$

can be expressed as [40]

$$\underset{\sim}{\omega} = \left[\cos\alpha \quad \sin\alpha e^{j\psi}\right]^T, \begin{cases} 0 \le \alpha \le \pi/2 \\ -\pi \le \psi \le \pi \end{cases} \tag{8}$$

where α determines the type of scattering mechanism, and ψ accounts for the phase relation. Substituting (5) into (1), the ADI for the polarimetric case (D_A^{Pol}) can be expressed as follows:

$$D_A^{\mathrm{Pol}} = \frac{\sqrt{\sum_{i=1}^{N}\left(\left|\underset{\sim}{\omega}^H K_i\right| - \overline{\left|\underset{\sim}{\omega}^H \underset{\sim}{K}\right|}\right)^2/N}}{\sum_{i=1}^{N}\left|\underset{\sim}{\omega}^H K_i\right|/N}. \tag{9}$$

According to (8), the polarimetric optimization problem is reduced to finding a suitable α and ψ in a finite and known range, so that (9) is minimized. To find an initial value of parameters that corresponds to a value close to the global minimum of the ADI, a grid with step size of 5° for both parameters is first defined. The Broyden–Fletcher–Goldfarb–Shanno (BFGS) algorithm [41], which is a quasi-Newton method for constrained nonlinear optimization, is then used to minimize the index.

D. *Classification of the Scattering Mechanism*

For a dual-polarized SAR image, each pixel is represented by a 2×2 coherency matrix, which is nonnegative definite and Hermitian. The eigenvalue decomposition of the coherency matrix is used to compute the polarimetric entropy H and the scattering angle α. H is defined as a measure of randomness in the polarization of the backscattered signal, and α is related to the physical scattering mechanism. They are defined as follows [42]:

$$H = \sum_{i=1}^{2} P_i \log_2 P_i \quad \text{and } \alpha = \sum_{i=1}^{2} P_i \alpha_i \tag{10}$$

where $P_i = \lambda_i/(\lambda_1 + \lambda_2)$, λ is the eigenvalue of the coherency matrix and α_i corresponds to the orthonormal eigenvectors of the coherency matrix.

Having obtained entropy and alpha values for each coherency matrix, an H-alpha plane as described by Cloude and Pottier [43] and Cloude [44] can be achieved. The H-alpha plane can be used to interpret and classify the scattering mechanism of the subsurface targets.

III. Dataset and Study Area

A total of 50 dual-polarization (VV–VH) SLC images of Sentinel-1 acquired in interferometric wide swath mode over Trondheim city covering January 2015–December 2016 are used to evaluate the optimization method described in Section II-C. The azimuth and range resolutions of Sentinel-1 data are approximately 22 and 2.65 m, with pixel dimensions of approximately 13.90 and 2.33 m in azimuth and range directions, respectively. The images are acquired in an ascending track, with a mean incidence angle of approximately 33°. Each image swath consists of three subswaths. The processing has been applied over a 990×2700 portion of the first subswath of the images. Fig. 1 illustrates the outline of the processed section superimposed over the aerial image of Trondheim.

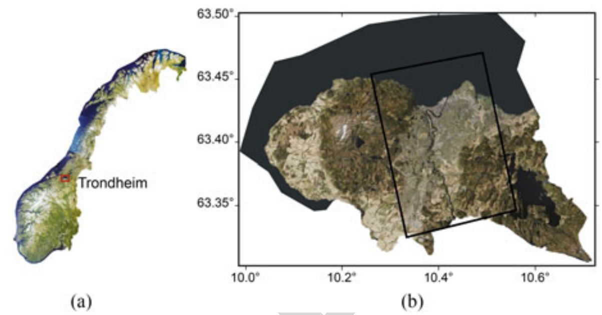

Fig. 1. (a) Location of Trondheim city in central Norway indicated by the red rectangle. (b) Aerial image of the study area (www.Norgeskart.no). The black rectangle shows the frame of Sentinel-1 sensor processed in this study.

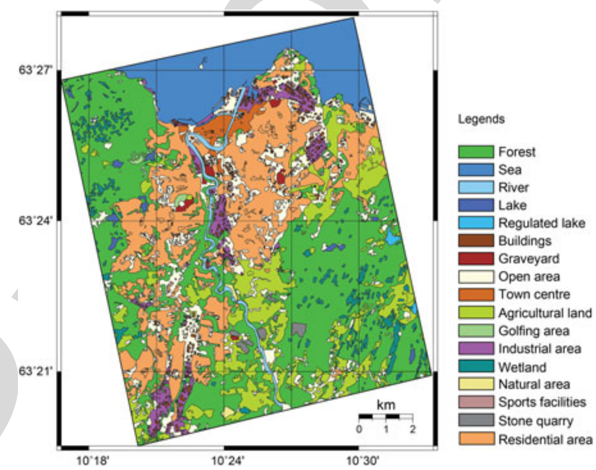

Fig. 2. Land use map of the study area (www.geonorge.no).

Trondheim city is located in central Norway. According to the Norwegian mapping authority, Kartverket, the most represented land use classes within the processed frame are vegetation, urban areas, and water bodies, covering ∼47%, ∼38%, and ∼15% of the region of interest, respectively (see Fig. 2). The urban classes mainly comprise commercial, industrial, and residential units. The commercial units, which are located in the town center, have a large (length, width, and height) and dense element of shops and service buildings. The buildings have predominantly two or more storeys with metallic constituents (having a strong reflection). Industrial regions consist of the largest buildings, developed or undeveloped, used for industrial purposes, installations for water supply, waste handling and cleaning, power plants, transformer substation, etc. In contrast to the commercial and industrial units, residential houses are smaller in size, with single- or two-storey rectangular buildings. In addition, they have been constructed mainly with wood and have tilted roofs. The buildings, for the most part, are closer than 50 m apart.

IV. Processing Strategy

Fig. 3 illustrates the flowchart of the processing developed in this paper. It includes three steps: first, preprocessing, second,

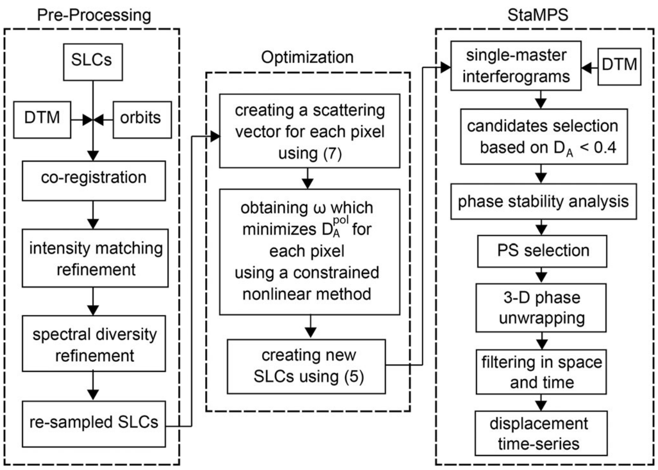

Fig. 3. Flowchart of the overall processing used in this study.

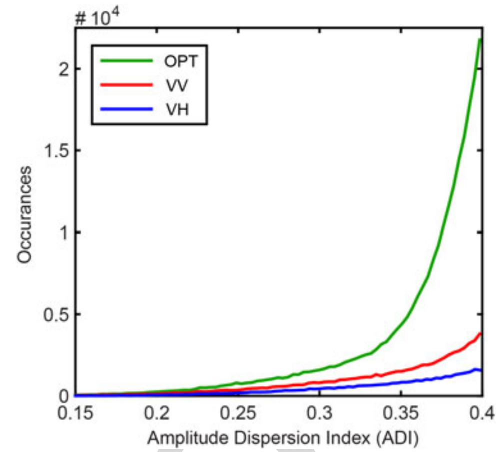

Fig. 4. Histograms of the ADI less than the considered PSC threshold (0.4) for optimum (green), VV (red), and VH (blue) channels.

optimization, and third, the PS-InSAR processing. These steps are briefly described in the following.

The scene acquired on July 25, 2015 is used as the super-master image to minimize the spatial and temporal baselines of the interferograms to be formed. The slave images are coregistered and resampled to the reference geometry (the master image) using GAMMA software [45]. In GAMMA software, the first step of the Sentinel-1 SLC co-registration procedure is based on the orbit geometry and terrain height. In the next step, the refinement of the coregistration is done iteratively using the intensity matching and the spectral diversity methods, in which the matching refinement iterates until the azimuth correction determined is better than 0.01 pixel. After reaching this quality, the spectral diversity method iterates until the azimuth correction determined is <0.0005 pixel [46].

Having made this, the precisely resampled SLCs are available. The next step is to find the projection vector that provides the minimized value of the ADI using the BFGS algorithm. Afterward, the SLCs are reproduced in optimized scattering mechanism by using (5), and the optimal interferograms are generated. To create the interferograms, we used the repeat-pass technique implemented in DORIS software [47] to be able to process further steps of the PS-InSAR analysis in StaMPS software. Initial topographic phase components are subtracted from the interferograms and, then, geocoding is done using digital terrain model at 40-m resolution provided by the Norwegian Mapping Authority.

The new differential interferograms, available after the optimization, are used as input data for the PS-InSAR algorithm in StaMPS software. The ADI threshold of 0.4 is set to identify the initial set of the PSC pixels, as thresholding on the ADI ≤ 0.4 improves computational times, reduces the data by an order of magnitude, and includes most of the PS points [48].

V. Results and Discussions

A. Dual-Polarized Versus Single-Polarized PS-InSAR

The datasets were processed using both the standard single-polarized PS-InSAR approach in StaMPS software and the described algorithm in Section IV. Fig. 4 shows the histograms of the ADI less than 0.4 (the threshold) obtained for VV, VH, and the optimum channels. As it can be seen in the figure, compared to the conventional channels, the optimum channel has significantly improved the amplitude stability. We find about 2.5 and 5.5 times as much the number of PSCs in the optimum channel as compared to that provided by single-polarized VV and VH data, respectively.

After achieving improvement in the number of candidates as a result of the optimization, phase-stability analysis was iteratively done on the identified PSCs, and the PS points were finally selected. The results from the processing of VH, VV, and optimum channels consist of approximately 37 700, 60 730, and 108 000 PS points in the processed region of interest, respectively. From the results, we find that the final number of PS points obtained by the processing of the optimum channel has been increased by approximately 186% and 78% as compared to the standard processing by VH and VV channels, respectively.

B. PS Density in Different Land Use

To illustrate the spatial patterns of the PS density-variation among the channels, the PS density obtained by the VV and VH channels have been subtracted from that, which has been obtained by the optimum channel. The results have been represented in Fig. 5(a) and (b), respectively. Clearly recognizable is that the PS density has been significantly increased across the whole processed area, but with different variations over the urban units. The maximum PS density of $\sim$2698 PS/km^2, $\sim$4427 PS/km^2, and $\sim$6942 PS/km^2, in the processed region of interest, is achieved from VH, VV, and the optimum channel, respectively.

Fig. 6 provides further insight into our findings by presenting the number of PSC and PS points detected using the conventional and optimum channels in urban and nonurban units. According to the figure, the number of PSC points in urban and nonurban units derived by the optimum channel has increased by about 3.7 and 22.9 times, respectively, as compared to the VH channel. The number of final PS points has increased by

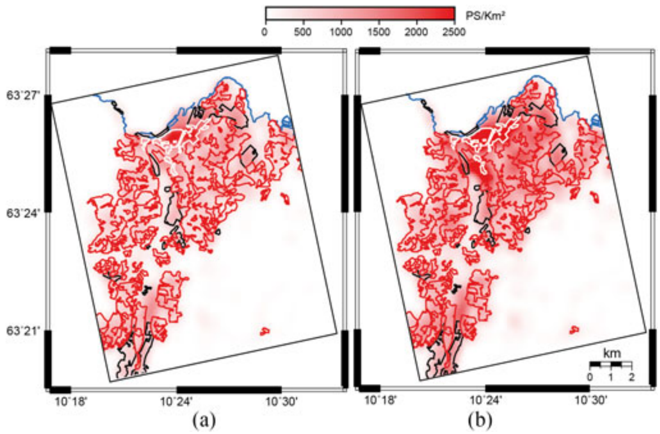

Fig. 5. Differences in the PS density between the optimum channel and (a) VV and (b) VH channels. The border of the commercial, residential, and industrial clusters have been illustrated by white, red, and black polygons, respectively.

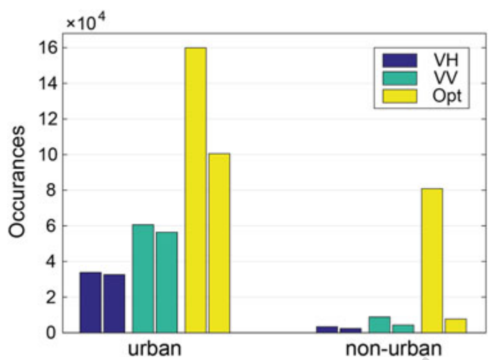

Fig. 6. Number of detected PSC (left bars) and PS (right bars) pixels detected in VH (blue), VV (green), and optimum (yellow) channels.

TABLE I
EXTRA PSC/PS PIXELS DETECTED USING THE OPTIMUM CHANNEL, AS COMPARED TO VH AND VV CHANNELS

	PSC		PS	
	VH [%]	VV [%]	VH [%]	VV [%]
urban	373	164	209	78
Non-urban	2289	818	234	79
total	547	247	186	78

about 2.1 times in urban and 2.3 times in nonurban units as compared to the VH channel. The increment in the PSC with respect to the VV channel is about 1.6 times in the urban and about 8.2 times in nonurban units. The number of final PS points in the optimum channel has increased by about 0.78 times in both units as compared to the VV channel. Table I summarizes the percentage of extra PSC and PS pixels detected using the polarimetric data in both units.

C. Scattering Mechanism of Urban Units

To interpret the scattering mechanism of the subsurface targets in the urban classes, we used H-alpha decomposition; the distribution of H-alpha for individual urban classes is plotted

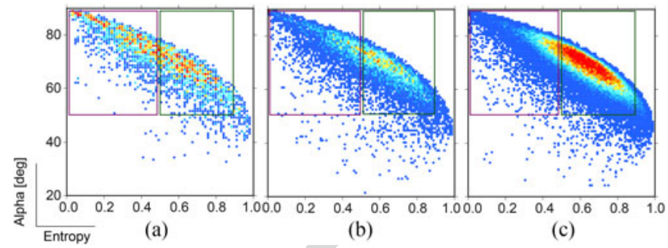

Fig. 7. H_alpha scatterplot for (a) commercial, (b) industrial, and (c) residential units, obtained from dual polarimetric decomposition of the Sentinel-1 image. The plots have been color-coded by the smoothed density of the points, in which the blue points have the minimum and the red points have the maximum density.

in Fig. 7. We empirically obtained that the scatterings with the entropy of less than 0.5 and the alpha of higher than 50° (the purple rectangle in the figure) correspond to low entropy multiple-scattering events (double-bounce scattering), such as provided by isolated dielectric and metallic dihedral scatterers. In addition, the scatterings with the entropy of 0.5–0.9 and the alpha of higher than 50° (the green rectangle in the figure) correspond to medium entropy multiple scattering, such as building and forested regions. Q2

From Fig. 7, it can be seen that in the commercial unit, the number of double-bounce scatterers are dominant. From the commercial unit to the residential unit, the distributions become more concentrated at the medium entropy. In other words, the number of double-bounce scatterers reduces, whereas the number of targets with medium-entropy scattering increases.

Over the urban units, the density in the residential areas (the red polygons in Fig. 5) has been increased, on average, from $\sim$780 PS/ km^2 in VV and $\sim$420 PS/ km^2 in VH to $\sim$1410 PS/ km^2 in the optimum channel. In the industrial units (the black polygons in Fig. 5), the density has been risen, on average, from $\sim$1090 PS/ km^2 in VV and $\sim$700 PS/ km^2 in VH to $\sim$1940 PS/ km^2 in the optimum channel. For the commercial areas (depicted by white polygons in Fig. 5), it has been increased, on average, from $\sim$2710 PS/ km^2 in VV and $\sim$1710 PS/ km^2 in VH to $\sim$4550 PS/ km^2 in the optimum channel. The highest density is achieved in commercial areas, which contain mostly double-bounce targets [see Fig. 7(a)], whereas the lowest density is obtained in residential areas, which contain mainly scatterers with medium entropy [see Fig. 7(c)]. Comparing the increment in densities shows that best improvement (an increase of about 80% and 235% compared to VV and VH, respectively) is achieved in residential areas, while the least increment (an increase of about 68% and 166% compared to VV and VH, respectively) is obtained in commercial areas.

D. Comparison Between the Scattering Angles

Comparing the optimum scattering mechanism derived from the optimization approach [see Fig. 8(a)] with the dominant scattering mechanism derived from the H-alpha decomposition [see Fig. 8(b)] shows that there is almost similar pattern between them, especially in areas, which have low entropy [see Fig. 8(c)]. To investigate the correlation between the scattering mechanisms, we extracted for each PS point, i.e., the optimum

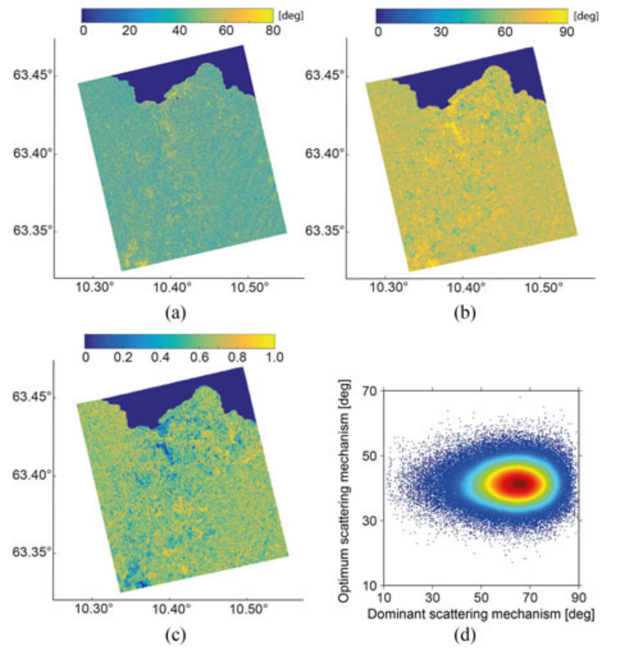

Fig. 8. (a) Optimum scattering mechanism (alpha) derived from the ADI optimization approach. (b) Dominant scattering mechanisms. (c) Entropy derived from the H-alpha decomposition. (d) Scatterplot of (a) versus (b) at the location of the PS points, color-coded by the smoothed density of the points in which blue to red color shows the lowest and the highest densities.

scattering mechanism and the dominant scattering mechanism values inside a circle with 20 m radius centered at the location of each PS point, and plotted the values in Fig. 8(d). It can be seen that, generally, the optimum alpha derived by the ADI optimization approach took lower values than the dominant alpha. The dominant alpha ranges between 10° and 90°, whereas the optimum alpha varies between 20° and 60°. However, the majority of points are concentrated in the dominant alpha values of 55°–75° and the optimum alpha values of 35°–45°, expressing that there is a good correlation in the areas with double-bounce scatterers.

Part of the differences might be caused by the fact that the ADI is computed for single-look data, so the optimum alpha derived by the ADI optimization approach is more sensitive to polarimetric features inside the resolution cell. Since the alpha derived from the decomposition is computed over a spatial window, it is defined by the averaged features of an extended area [23].

E. PSC Versus PS

In most part of the processed area, the magnitude of the VH channel is less than half of the magnitude of the VV channel. It even reaches to less than 0.1 in areas with double-bounce scattering targets. They may even degrade due to noise, and their dispersion may increase because of the existence of the different level of noise in each acquisition. As a result, the classical PS-InSAR analysis, which relies on targets with low-amplitude dispersion, is limited to select the pixels with low amplitude. Our results show that, using the optimization process, we can handle this problem and incorporate information that exist in VH in the time-series analysis, which otherwise will be lost due to the low amplitude in VH. Consequently, the number of PSC points as well as the number and density of PS points increase noticeably.

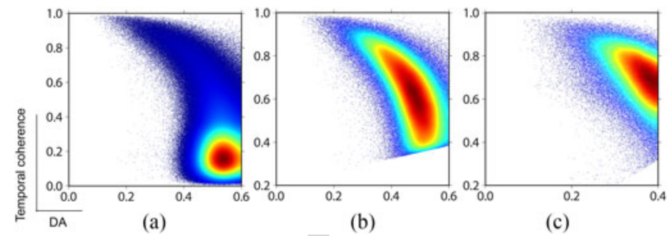

Fig. 9. Scatterplot of the distribution of the ADI versus the temporal coherence of the (a) PSC and (b) final PS points obtained by the ADI threshold of 0.6 on the VV channel, and (c) final PS points obtained by the optimum channel. The plots are color-coded by the smoothed density of the points in which blue to red color shows the lowest and the highest densities.

However, comparing the number of PSs with PSCs in urban areas shows a reduction of about 4%, 7%, and 37% of the candidates derived by VH, VV, and optimum channels, respectively, after phase-stability analysis. For nonurban areas, the reduction is about 32% in VH, 50% in VV, and 90% in the optimum channel. Therefore, using the optimization process, we can benefit from the VH channel despite of its low amplitude, and increase the number of PSC. However, after applying the phase-stability analysis, many of them are dropped (will be discussed in Section V-F). It is concluded that the amplitude dispersion analysis criterion alone is not sufficient for PS selection, and the phase analysis should be performed to better estimate the phase stability of the PSC points.

F. ADI Thresholding

Another way to increase the number of PS points is taking a less-constraining ADI threshold for initial selection. We considered thresholding on ADI ≤0.6 on the VV channel, without optimization, and compared the result with that obtained by the optimization method. Fig. 9(a) shows the distribution of the ADI versus the temporal coherence of the PS candidates, color-coded by the smoothed density of the points in which blue to red color shows the lowest and highest densities. As it can be seen in the figure, the majority of points have the ADI between 0.4 and 0.6, and the temporal coherence of less than 0.4. Fig. 9(b) shows the same scatterplot for the final PS points. It shows that most of the final PS points have the ADI between 0.4 and 0.55 and the temporal coherence of 0.4–0.8. Using this approach, 86.5% of the PSC points are discarded after the phase analysis.

In Fig. 9(c), we plotted the same distribution for the final PS points obtained by the optimum channel. Most of the final PS points have the ADI of 0.3–0.4 and the temporal coherence of 0.6–0.8. Comparing the two plots shows that, using optimization method, the final PS points have better coherence. Looking at the position of the final PS points selected by increasing the ADI threshold shows that, several points have been selected over the forest areas, which may affect the reliability of phase unwrapping.

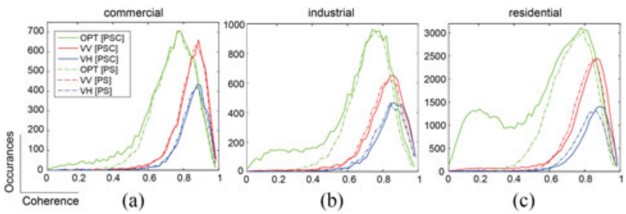

Fig. 10. Histograms of the temporal coherence values of the PSC (solid curves) and PS (dashed curves) points for optimum (green), VV (red), and VH (blue) channels in the commercial, industrial, and residential units.

G. Temporal Coherence

Fig. 10 shows the histograms of the temporal coherence values of the PSC (solid curves) and PS (dashed curves) points for the different urban units derived by the optimum (green), VV (red) and VH (blue) channels. From commercial to residential, as the number of targets with double-bounce scattering decreases, the distribution is inclined toward the double-peaks distribution. Further investigations showed that the PSCs in the left part of the distributions in industrial and residential areas are associated with pixels having high ADI (0.3–0.4), which have been selected by candidates more likely from vegetation areas. However, they have been discarded after the phase-stability analysis due to low-temporal coherence.

Comparing the distribution of the optimum and VV channels shows that the width of the distributions has increased with this method. However, the mode values changed from approximately 0.85 to 0.75, as compared to the conventional channel distributions. In addition, on the one hand, the method increases the number of PS points having the coherence of less than $\sim$0.85, but on the other hand, decreases the coherence for the points, which have the coherence of more than $\sim$0.85 in the VV channel. We clearly see that the decrease has been amplified in commercial areas and reduced in residential areas. In other words, the lessening of the high-temporal coherence values has been adversely affected by the targets type.

H. Consistency of Results

To assess the consistency between the PS-InSAR results obtained from the optimum, VV, and VH channels, it is necessary to derive the displacement rates at the same locations for the datasets. For this purpose, we extracted the rates inside a circle with 150 m radius, centered at the location of the PS pixels in the VH result, which has the lowest density among the results. To illustrate the correlations between the results, we plotted with positions given by the line of sight (LOS) displacement rate derived by the VV and VH channels, and color corresponding to the LOS rate derived by the optimum channel [see Fig. 11(a)]. The figure shows that the results are in general agreement with each other. The correlation coefficients of 0.85 and 0.92 were observed between the optimum results and VH and VV results, respectively, indicating the general consistency of the results.

As a result of the PS-InSAR processing, the LOS time-series displacement is acquired for each PS points. For comparison of the displacements in time, we plotted the mean LOS results with the associated standard deviations for PS points within a circle

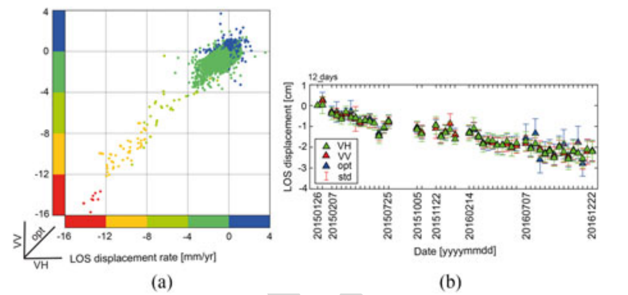

Fig. 11. (a) Scatterplot of the LOS rate derived by the VV channel against the VH channel. The color of PS points corresponds to the LOS rate derived by the optimum channel. (b) Time-series displacement of one PS point in the LOS direction is obtained by VH, VV, and optimum channels, represented by green, red, and blue triangles, respectively, with their associated standard deviations.

with 50 m radius centered at the area with maximum LOS displacement rate [see Fig. 11(b)]. The figure, in general, indicates a good agreement between the results. Some discrepancies with maximum value of 5 mm can be seen between the optimum result and two other results. However, the differences are less than their associated standard deviations. This might be caused by different PS densities, which fall into the defined circle.

VI. Conclusion

We implemented a polarimetric optimization approach on Sentinel-1 dual-polarization (VV–VH) images to improve the PS-InSAR method. In general, the amplitude of the VH channel is one order of magnitude smaller than that of the VV channel. However, using the optimization method, we can incorporate the information that exists in the VH channel into the time-series analysis, which otherwise is lost due to its low amplitude. As a result of this approach, we achieved the general increment of about 78% and 186% in the number of PS points, with respect to the VV and VH channels, respectively. Further analysis on the efficiency of the method across urban units revealed that the improvement in the areas with double-bounce scatterers is less than other scatterers. In addition, the method decreases the temporal-coherence values of PS points (PS points with the coherence values of higher than 0.85) in areas with double-bounce scattering targets. We also analyzed the correlation between the LOS displacement rates and the time-series obtained by the optimum and the conventional channels, and found high correlations between them, which indicates the general consistency of the results.

Acknowledgment

The land use map and the digital terrain model have been provided by the Norwegian Mapping Authority.

References

[1] M. Esmaeili and M. Motagh, “Improved persistent scatterer analysis using amplitude dispersion index optimization of dual polarimetry data,” *ISPRS J. Photogrammetry Remote Sens.*, vol. 117, pp. 108–114, 2016.

[2] C. Colesanti, A. Ferretti, F. Novali, C. Prati, and F. Rocca, “SAR monitoring of progressive and seasonal ground deformation using the permanent scatterers technique,” *IEEE Trans. Geosci. Remote Sens.*, vol. 41, no. 7, pp. 1685–1701, Aug. 2003.

[3] M. Crosetto, E. Biescas, J. Duro, J. Closa, and A. Arnaud, “Generation of advanced ERS and Envisat interferometric SAR products using the stable point network technique,” *Photogramm. Eng. Remote Sens.*, vol. 74, no. 4, pp. 443–450, 2008.

[4] A. Ferretti, C. Prati, and F. Rocca, “Nonlinear subsidence rate estimation using permanent scatterers in differential SAR interferometry,” *IEEE Trans. Geosci. Remote Sens.*, vol. 38, no. 5, pp. 2202–2212, Sep. 2000.

[5] A. Ferretti, C. Prati, and F. Rocca, “Permanent scatterers in SAR interferometry,” *IEEE Trans. Geosci. Remote Sens.*, vol. 39, no. 1, pp. 8–20, Jan. 2001.

[6] A. Hooper, H. Zebker, P. Segall, and B. Kampes, “A new method for measuring deformation on volcanoes and other natural terrains using InSAR persistent scatterers,” *Geophys. Res. Lett.*, vol. 31, no. 23, 2004, Art. no. L23611.

[7] B. M. Kampes and R. F. Hanssen, “Ambiguity resolution for permanent scatterer interferometry,” *IEEE Trans. Geosci. Remote Sens.*, vol. 42, no. 11, pp. 2446–2453, Nov. 2004.

[8] O. Mora, J. J. Mallorqui, and A. Broquetas, “Linear and nonlinear terrain deformation maps from a reduced set of interferometric SAR images,” *IEEE Trans. Geosci. Remote Sens.*, vol. 41, no. 10, pp. 2243–2253, Oct. 2003.

[9] F. Cigna, R. Lasaponara, N. Masini, P. Milillo, and D. Tapete, “Persistent scatterer interferometry processing of COSMO-SkyMed StripMap HIMAGE time series to depict deformation of the historic centre of Rome, Italy,” *Remote Sens.*, vol. 6, no. 12, pp. 12593–12618, 2014.

[10] P. Teatini, G. Gambolati, M. Ferronato, A. T. Settari, and D. Walters, “Land uplift due to subsurface fluid injection,” *J. Geodynamics*, vol. 51, no. 1, pp. 1–16, 2011.

[11] C. Meisina *et al.*, “Geological interpretation of PSInSAR data at regional scale,” *Sensors*, vol. 8, no. 11, pp. 7469–7492, 2008.

[12] V. Tofani, F. Raspini, F. Catani, and N. Casagli, “Persistent scatterer interferometry (PSI) technique for landslide characterization and monitoring,” *Remote Sens.*, vol. 5, no. 3, pp. 1045–1065, 2013.

[13] R. Bürgmann, G. Hilley, A. Ferretti, and F. Novali, “Resolving vertical tectonics in the San Francisco bay area from permanent scatterer InSAR and GPS analysis,” *Geology*, vol. 34, no. 3, pp. 221–224, 2006.

[14] E. Lagios *et al.*, “Combined seismicity pattern analysis, DGPS and PSInSAR studies in the broader area of Cephalonia (Greece),” *Tectonophysics*, vol. 524, pp. 43–58, 2012.

[15] M. Motagh, J. Hoffmann, B. Kampes, M. Baes, and J. Zschau, “Strain accumulation across the Gazikoy–Saros segment of the North Anatolian fault inferred from persistent scatterer interferometry and GPS measurements,” *Earth Planet. Sci. Lett.*, vol. 255, no. 3, pp. 432–444, 2007.

[16] A. Peltier *et al.,* “PSInSAR as a new tool to monitor pre-eruptive volcano ground deformation: Validation using GPS measurements on Piton de la Fournaise,” *Geophys. Res. Lett.*, vol. 37, no. 12, 2010, Art. no. L12301.

[17] P. Berardino, G. Fornaro, R. Lanari, and E. Sansosti, “A new algorithm for surface deformation monitoring based on small baseline differential SAR interferograms,” *IEEE Trans. Geosci. Remote Sens.*, vol. 40, no. 11, pp. 2375–2383, Nov. 2002.

[18] S. R. Cloude and K. P. Papathanassiou, “Polarimetric SAR interferometry,” *IEEE Trans. Geosci. Remote Sens.*, vol. 36, no. 5, pp. 1551–1565, Sep. 1998.

[19] E. Colin, C. Titin-Schnaider, and W. Tabbara, “An interferometric coherence optimization method in radar polarimetry for high-resolution imagery,” *IEEE Trans. Geosci. Remote Sens.*, vol. 44, no. 1, pp. 167–175, Jan. 2006.

[20] A. G. Mullissa, V. Tolpekin, A. Stein, and D. Perissin, “Polarimetric differential SAR interferometry in an arid natural environment,” *Int. J. Appl. Earth Observation Geoinformation*, vol. 59, pp. 9–18, 2017.

[21] M. Neumann, L. Ferro-Famil, and A. Reigber, “Multibaseline polarimetric SAR interferometry coherence optimization,” *IEEE Geosci. Remote Sens. Lett.*, vol. 5, no. 1, pp. 93–97, Jan. 2008.

[22] R. Iglesias *et al.,* “Phase quality optimization in polarimetric differential SAR interferometry,” *IEEE Trans. Geosci. Remote Sens.*, vol. 52, no. 5, pp. 2875–2888, May 2014.

[23] V. D. Navarro-Sanchez and J. M. Lopez-Sanchez, “Improvement of persistent-scatterer interferometry performance by means of a polarimetric optimization,” *IEEE Geosci. Remote Sens. Lett.*, vol. 9, no. 4, pp. 609–613, Jul. 2012.

[24] L. Pipia *et al.*, “Polarimetric differential SAR interferometry: First results with ground-based measurements,” *IEEE Geosci. Remote Sens. Lett.*, vol. 6, no. 1, pp. 167–171, Jan. 2009.

[25] V. D. Navarro-Sanchez, J. M. Lopez-Sanchez, and L. Ferro-Famil, “Polarimetric approaches for persistent scatterers interferometry,” *IEEE Trans. Geosci. Remote Sens.*, vol. 52, no. 3, pp. 1667–1676, Mar. 2014.

[26] B. Wu, L. Tong, Y. Chen, and L. He, “New methods in multibaseline polarimetric SAR interferometry coherence optimization,” *IEEE Geosci. Remote Sens. Lett.*, vol. 12, no. 10, pp. 2016–2020, Oct. 2015.

[27] R. Iglesias *et al.,* “Polarimetric optimization of temporal sublook coherence for DInSAR applications,” *IEEE Geosci. Remote Sens. Lett.*, vol. 12, no. 1, pp. 87–91, Jan. 2015.

[28] D. Monells, J. Mallorqui, G. Centolanza, and C. Lopez-Martinez, “Application of polarimetric techniques in DInSAR processing for space borne subsidence monitoring,” in *Proc. Sci. Appl. SAR Polarimetry Polarimetric Interferometry*, 2011, vol. 695. Q3

[29] K. Ishitsuka, T. Matsuoka, and M. Tamura, “Persistent scatterer selection incorporating polarimetric SAR interferograms based on maximum likelihood theory,” *IEEE Trans. Geosci. Remote Sens.*, vol. 55, no. 1, pp. 38–50, Jan. 2017.

[30] S. Samsonov and K. Tiampo, “Polarization phase difference analysis for selection of persistent scatterers in SAR interferometry,” *IEEE Geosci. Remote Sens. Lett.*, vol. 8, no. 2, pp. 331–335, Mar. 2011.

[31] S. Alipour, K. F. Tiampo, S. V. Samsonov, and P. J. González, “Short-term surface deformation on the Northern Hayward fault, CA, and nearby landslides using polarimetric SAR interferometry (PolInSAR),” *Pure Appl. Geophys.*, vol. 172, no. 8, pp. 2179–2193, 2015.

[32] M. Esmaeili, M. Motagh, and A. Hooper, “Application of dual-polarimetry SAR images in multitemporal InSAR processing,” *IEEE Geosci. Remote Sens. Lett.*, vol. 14, no. 9, pp. 1489–1493, Sep. 2017.

[33] V. D. Navarro-Sanchez and J. M. Lopez-Sanchez, “Spatial adaptive speckle filtering driven by temporal polarimetric statistics and its application to PSI,” *IEEE Trans. Geosci. Remote Sens.*, vol. 52, no. 8, pp. 4548–4557, Aug. 2014.

[34] R. M. Goldstein and C. L. Werner, “Radar interferogram filtering for geophysical applications,” *Geophys. Res. Lett.*, vol. 25, no. 21, pp. 4035–4038, 1998.

[35] A. Hooper, P. Segall, and H. Zebker, “Persistent scatterer interferometric synthetic aperture radar for crustal deformation analysis, with application to Volcán Alcedo, Galápagos,” *J. Geophys. Res., Solid Earth*, vol. 112, no. B7, 2007, Art. no. B07407.

[36] A. Hooper and H. A. Zebker, “Phase unwrapping in three dimensions with application to InSAR time series,” *J. Opt. Soc. Amer. A*, vol. 24, no. 9, pp. 2737–2747, 2007.

[37] S. Cloude and K. Papathanassiou, “Polarimetric optimisation in radar interferometry,” *Electron. Lett.*, vol. 33, no. 13, pp. 1176–1178, 1997.

[38] K. Ji and Y. Wu, “Scattering mechanism extraction by a modified Cloude-Pottier decomposition for dual polarization SAR,” *Remote Sens.*, vol. 7, no. 6, pp. 7447–7470, 2015.

[39] A. G. Mullissa, D. Perissin, V. A. Tolpekin, and A. Stein, “Polarimetry-based distributed scatterer processing method for PSI applications,” *IEEE Trans. Geosci. Remote Sens.*, vol. 56, no. 6, pp. 3371–3382, Jun. 2018.

[40] V. D. Navarro-Sanchez, J. M. Lopez-Sanchez, and F. Vicente-Guijalba, “A contribution of polarimetry to satellite differential SAR interferometry: Increasing the number of pixel candidates,” *IEEE Geosci. Remote Sens. Lett.*, vol. 7, no. 2, pp. 276–280, Apr. 2010.

[41] R. Battiti and F. Masulli, “BFGS optimization for faster and automated supervised learning,” in *Proc. Int. Neural Netw. Conf.*, Springer, 1990, pp. 757–760.

[42] S. R. Cloude and E. Pottier, “A review of target decomposition theorems in radar polarimetry,” *IEEE Trans. Geosci. Remote Sens.*, vol. 34, no. 2, pp. 498–518, Mar. 1996.

[43] S. R. Cloude and E. Pottier, “An entropy based classification scheme for land applications of polarimetric SAR,” *IEEE Trans. Geosci. Remote Sensing*, vol. 35, no. 1, pp. 68–78, Jan. 1997.

[44] S. Cloude, “The dual polarization entropy/alpha decomposition: A PALSAR case study,” in *Proc. Sci. Appl. SAR Polarimetry Polarimetric Interferometry*, 2007, vol. 644.

[45] U. Wegmüller and C. Werner, “Gamma SAR processor and interferometry software,” in *Proc. 3rd ERS Symp.*, 1997, pp. 1687–1692.

[46] R. Scheiber and A. Moreira, “Coregistration of interferometric SAR images using spectral diversity,” *IEEE Trans. Geosci. Remote Sens.*, vol. 38, no. 5, pp. 2179–2191, Sep. 2000.

[47] B. M. Kampes, R. F. Hanssen, and Z. Perski, “Radar interferometry with public domain tools,” in *Proc. FRINGE*, 2003, vol. 3.

[48] A. J. Hooper, “Persistent scatter radar interferometry for crustal deformation studies and modeling of volcanic deformation,” Ph.D. dissertations, Stanford Univ., Sanford, CA, USA, 2006. Q4

Authors’ photographs and biographies not available at the time of publication.

GENERAL INSTRUCTIONS

- Authors: When accessing and uploading your corrections at the Author Gateway, please note we cannot accept new source files as corrections for your paper. Do not send new Latex, Word, or PDF files, as we cannot simply “overwrite” your paper. Please submit your corrections as an annotated PDF or as clearly written list of corrections, with location in paper. You can also upload revised graphics to the Gateway.
- Authors: Please note that once you click “approve with no changes,” the proofing process is now complete and your paper will be sent for final publication and printing. Once your paper is posted on Xplore, it is considered final and the article of record. No further changes will be allowed at this point so please ensure scrutiny of your final proof.
- Authors: Unless invited or otherwise informed, a mandatory Excessive Paper Length charge of $200.00 per page (beginning with page 7 and beyond) is required for papers in excess of six (6) printed pages for JSTARS. If you have any questions regarding overlength page charges, need an invoice, or have any other billing questions, please contact reprints@ieee.org as they handle these billing requests.

QUERIES

Q1. Author: Please confirm or add details for any funding or financial support for the research of this article.
Q2. Author: Please check whether the edits made in the sentence “To interpret the scattering mechanism of the subsurface . . . ” retain the intended sense.
Q3. Author: Please provide page numbers for [28], [44], and [47].
Q4. Author: Please provide name of the department in Ref. [48].

Persistent Scatterer Analysis Using Dual-Polarization Sentinel-1 Data: Contribution From VH Channel

Roghayeh Shamshiri, Hossein Nahavandchi, and Mahdi Motagh

***Abstract*—The regular acquisition and relatively short revisit time of Sentinel-1 satellite improve the capability of a persistent scatterer interferometric synthetic aperture radar (PS-InSAR) as a suitable geodetic method of choice for measuring ground surface deformation in space and time. The SAR instrument aboard the Sentinel-1 satellite supports operation in dual polarization (HH–HV, VV–VH), which can be used to increase the spatial density of measurement points through the polarimetric optimization method. This study evaluates the improvement in displacement mapping by incorporating the information obtained from the VH channel of Sentinel-1 data into the PS-InSAR analysis. The method that has shown great success with different polarimetric data performs a search over the available polarimetric space in order to find a linear combination of polarization states, which yields the optimum PS selection criterion using the amplitude dispersion index (ADI) criterion. We applied the method to a dataset of 50 dual-polarized (VV–VH) Sentinel-1 images over Trondheim city in Norway. The results show overall increase of about 186% and 78% in the number of PS points with respect to the conventional channels of VH and VV, respectively. The study concludes that, using the ADI optimization, we can incorporate information from the VH channel into the PS-InSAR analysis, which otherwise is lost due to its low amplitude.**

***Index Terms*—Dual polarization, optimization, persistent scatterer interferometric synthetic aperture radar (PS-InSAR), sentinel-1.**

I. Introduction

PERSISTENT scatterer interferometric synthetic aperture radar (PS-InSAR) has proved to be a powerful geodetic technique to measure deformations of the earth's surface in space and time using a stack of synthetic aperture radar (SAR) images [1]–[7]. It has been widely used by the scientific community to measure the displacement related to subsidence/uplift [8], [9], landslide [10], [11], tectonic [12]–[14], and volcanoes [5], [15]. In order to minimize spatiotemporal decorrelation effects and other sources of errors, the PS-InSAR technique processes only those pixels, known as persistent scatterer (PS), that their decorrelation effects are negligible under certain quality criterion. The most commonly used criteria in the PS-InSAR method are coherence stability [7], [16] and the amplitude dispersion index (ADI) [4].

Traditionally, the PS-InSAR method has been formulated and applied to single-polarimetric SAR data because of the limitations of available multipolarimetric SAR images. However, the recent launch of new satellites with capability of multipolarimetric acquisition motivated researchers to develop new techniques based on the polarimetric optimization. The approach has been applied to optimize the coherence in differential InSAR (DInSAR) [17], [18]. Coherence optimization algorithms have been evaluated for copolar (HH–VV) and cross-polar channels (HH–HV), in addition to the quad-polarized ALOS data for the DInSAR analysis [19].

It has also been applied on a multibaseline InSAR [20]. In the context of multibaseline, a search over the available polarimetric space is performed to find a channel that optimizes the phase-stability criteria, which in turn increases the number of measurement points and consequently enhances the performance of the method. The approach has been implemented on the PS-InSAR method by optimizing the coherence stability and the ADI [21]–[24]. Navarro-Sanchez *et al.* implemented the polarimetric optimization for the ADI for copolar and cross-polar channels in addition to the quad-polarized RADARSAT-2 data for the PS-InSAR analysis [25]. The PS selection procedure has also been optimized using signal-to-noise ratio [26], the temporal sublook coherence [27], [28] criteria with dual/multipolarized data, maximum likelihood function [29], and phase-difference between copolarized components [30]. The efficiency of the approach has also been proved in the small baseline method [31], [32].

The recent launch of the Sentinel-1 mission with capability to obtain acquisitions on dual-polarized (HH–HV, VV–VH) channels can help improving PS-InSAR analyses by increasing the PS density. In general, having more than one polarimetric channel helps to increase the PS density, especially in urban areas [21]–[23], [33], in which each resolution cell has a single dominant scattering mechanism. However, the amplitude of the cross-polar measurements is generally smaller than that of the copolar channels. Therefore, they may suffer more degradation due to noise, and their information might be lost in a single-polarized time-series analysis. Using the optimization method, we can incorporate their information into displacement mapping.

Manuscript received September 4, 2017; revised January 10, 2018 and April 30, 2018; accepted May 31, 2018. This work was supported by the Norwegian University of Science and Technology. *(Corresponding author: Roghayeh Shamshiri.)*

R. Shamshiri and H. Nahavandchi are with the Department of Civil and Environmental Engineering, Norwegian University of Science and Technology, Trondheim 7491, Norway (e-mail: roghayeh.shamshiri@ntnu.no; hossein.nahavandchi@ntnu.no).

M. Motagh is with GFZ German Research Center for Geosciences, Potsdam 14473, Germany, and also with Leibniz University, Hannover 30167, Germany (e-mail: motagh@gfz-potsdam.de).

Color versions of one or more of the figures in this paper are available online at http://ieeexplore.ieee.org.

Digital Object Identifier 10.1109/JSTARS.2018.2848111

In this study, we exploit the polarimetric information available in Sentinel-1 data (VV–VH) to investigate how the contribution of the VH channel affects the improvement of the PS-InSAR method over urban areas. We apply the approach presented in the previously published paper [21], but utilized it for Sentinel-1, due to easy access to the dataset and its free availability. Our goal is to analyze the performance of the approach. Trondheim city, located in central Norway, has been chosen as a test area. The city consists of several types of targets, which help to investigate the PS density and the phase-quality variations better as a function of the target types. These have been focused particularly in this study.

II. Method

A. StaMPS

The PS-InSAR method implemented in StaMPS works based on the spatial correlation approach. First, for computational reasons, an initial set of PS candidates (PSCs) is identified based on the ADI, defined as the ratio between standard deviation (σ_a) and mean ($\bar{a}$) of the amplitudes [4]

$$D_A = \frac{\sigma_a}{\bar{a}} = \frac{\sqrt{\sum_{i=1}^{N}\left(|s_i| - \overline{|s|}\right)^2 / N}}{\sum_{i=1}^{N}|s_i| / N} \tag{1}$$

where s is a complex value of a single-look complex (SLC) pixel, $|s_i|$ is the amplitude of the pixel in the ith SLC, and N is the number of SLCs. The lower the ADI values, the higher the phase quality. Therefore, pixels with the ADI less than a predefined threshold are selected as PSC points.

In the next step, for each PSC in each differential interferograms ($\psi_{x,i}$), the spatially correlated terms ($\tilde{\psi}_{x,i}$) including deformation, atmospheric signal, orbital inaccuracies, and spatially correlated part of the topographic phase due to the digital elevation model (DEM) errors, are estimated using a combination of low-pass and adaptive (Goldstein) phase filters iteratively [34]. The spatially uncorrelated part of the topographic phase ($\Delta\hat{\psi}^{u}_{\theta,x,i}$), which is correlated with the perpendicular baseline, is estimated by least-squares inversion. The temporal coherence (γ_x) is then calculated from residuals as follows [35]:

$$\gamma_x = \frac{1}{N}\left|\sum_{i=1}^{N}\exp\left\{j\left(\psi_{x,i} - \tilde{\psi}_{x,i} - \Delta\hat{\psi}^{u}_{\theta,x,i}\right)\right\}\right|. \tag{2}$$

Contribution of each pixel is weighted based on its estimated temporal coherence, followed by the re-estimation of the DEM error and the temporal coherence. This algorithm is iterated several times until the root-mean-square change in the temporal coherence ceases to decrease. Then, pixels are selected as PS points, considering their amplitude dispersion as well as their final temporal coherence. Afterward, three-dimensional phase unwrapping is done on the PS points [36]. The unwrapped phase of PS points is filtered using high-pass filtering in time and a low-pass filtering in space to estimate the atmospheric and orbital errors. Subtracting these terms from the unwrapped phase of each PS leaves the ground deformation estimate. Further details regarding StaMPS can be found in the relevant literatures [5], [35].

B. Polarimetric SAR

A fully polarimetric SAR measures a complex scattering matrix S at each pixel, which describes the scattering process of a target

$$S = \begin{bmatrix} S_{\mathrm{hh}} & S_{\mathrm{vh}} \\ S_{\mathrm{vh}} & S_{\mathrm{vv}} \end{bmatrix}. \tag{3}$$

Using the Pauli basis [37], the corresponding scattering vector $\underline{K}$ can be derived for each resolution element as follows:

$$\underline{K} = \frac{1}{\sqrt{2}}\left[\, S_{\mathrm{hh}} + S_{\mathrm{vv}} \;\; S_{\mathrm{hh}} - S_{\mathrm{vv}} \;\; 2S_{\mathrm{vh}} \,\right]^{T} \tag{4}$$

where T is the transpose operator, and S_{hh}, S_{vv}, and S_{vh} are the elements of matrix S standing for the copolar channels and the cross-polar channel. By defining a unitary complex projection vector $\underline{\omega}$, it is possible to generate a complex scalar image by projecting the scattering vector of each pixel, i onto μ, as

$$\mu_i = \omega_i^{H}\underline{K}_{i} \tag{5}$$

where H denotes conjugate transpose operation.

Equation (5) suggests that the optimization can be performed by choosing suitable polarimetric states $\underline{\omega}$ for each pixel. There are two general approaches for the polarimetric optimization of multibaseline interferograms. These are multibaseline equal scattering mechanism (MB-ESM) and multibaseline multiple scattering mechanism (MB-MSM) [20]. An important point to note is that as the polarimetric properties of the scene are not changed between data acquisitions, a single polarimetric state, i.e., ESM, is used for all acquisitions [20].

C. Modification of the Formulas for Dual-Polarized Sentinel-1 Data

The formulations stated in Section II-B are proposed for the fully polarimetric SAR. In this section, they are modified to be used for analyzing the dual-polarized SAR images of Sentinel-1. The scattering matrix and the corresponding scattering vector of VH–VV are, respectively, (see, e.g., [38], eqs. (18) and (19)], [39], eq. (3)),

$$S = \begin{bmatrix} 0 & S_{\mathrm{vh}} \\ S_{\mathrm{vh}} & S_{\mathrm{vv}} \end{bmatrix} \tag{6}$$

and

$$\underline{K} = \frac{1}{\sqrt{2}}\left[\, S_{\mathrm{vv}} \;\; 2S_{\mathrm{vh}} \,\right]^{T}. \tag{7}$$

Following the method developed by Cloude and Papathanassiou [37], in which the polarimetric state $\underline{\omega}$ is derived as eigenvectors for coherence optimization, the reduced version of $\underline{\omega}$

can be expressed as [40]

$$\underset{\sim}{\omega} = \begin{bmatrix} \cos\alpha & \sin\alpha e^{j\psi} \end{bmatrix}^T, \begin{cases} 0 \le \alpha \le \pi/2 \\ -\pi \le \psi \le \pi \end{cases} \tag{8}$$

where α determines the type of scattering mechanism, and ψ accounts for the phase relation. Substituting (5) into (1), the ADI for the polarimetric case (D_A^{Pol}) can be expressed as follows:

$$D_A^{\mathrm{Pol}} = \frac{\sqrt{\sum_{i=1}^{N} \left(\left| \underset{\sim}{\omega}^H K_i \right| - \overline{\left| \underset{\sim}{\omega}^H \underset{\sim}{K} \right|} \right)^2 / N}}{\sum_{i=1}^{N} \left| \underset{\sim}{\omega}^H K_i \right| / N}. \tag{9}$$

According to (8), the polarimetric optimization problem is reduced to finding a suitable α and ψ in a finite and known range, so that (9) is minimized. To find an initial value of parameters that corresponds to a value close to the global minimum of the ADI, a grid with step size of 5° for both parameters is first defined. The Broyden–Fletcher–Goldfarb–Shanno (BFGS) algorithm [41], which is a quasi-Newton method for constrained nonlinear optimization, is then used to minimize the index.

D. Classification of the Scattering Mechanism

For a dual-polarized SAR image, each pixel is represented by a 2×2 coherency matrix, which is nonnegative definite and Hermitian. The eigenvalue decomposition of the coherency matrix is used to compute the polarimetric entropy H and the scattering angle α. H is defined as a measure of randomness in the polarization of the backscattered signal, and α is related to the physical scattering mechanism. They are defined as follows [42]:

$$H = \sum_{i=1}^{2} P_i \log_2 P_i \quad \text{and } \alpha = \sum_{i=1}^{2} P_i \alpha_i \tag{10}$$

where $P_i = \lambda_i/(\lambda_1 + \lambda_2)$, λ is the eigenvalue of the coherency matrix and α_i corresponds to the orthonormal eigenvectors of the coherency matrix.

Having obtained entropy and alpha values for each coherency matrix, an H-alpha plane as described by Cloude and Pottier [43] and Cloude [44] can be achieved. The H-alpha plane can be used to interpret and classify the scattering mechanism of the subsurface targets.

III. Dataset and Study Area

A total of 50 dual-polarization (VV–VH) SLC images of Sentinel-1 acquired in interferometric wide swath mode over Trondheim city covering January 2015–December 2016 are used to evaluate the optimization method described in Section II-C. The azimuth and range resolutions of Sentinel-1 data are approximately 22 and 2.65 m, with pixel dimensions of approximately 13.90 and 2.33 m in azimuth and range directions, respectively. The images are acquired in an ascending track, with a mean incidence angle of approximately 33°. Each image swath consists of three subswaths. The processing has been applied over a 990×2700 portion of the first subswath of the images. Fig. 1 illustrates the outline of the processed section superimposed over the aerial image of Trondheim.

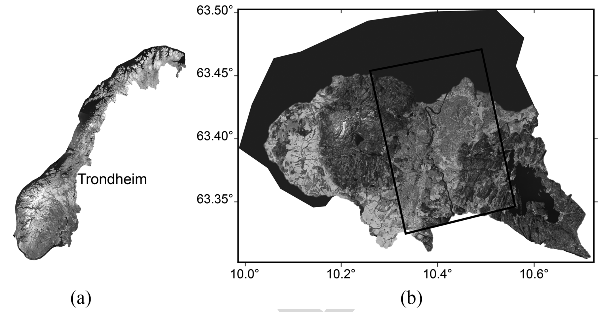

Fig. 1. (a) Location of Trondheim city in central Norway indicated by the red rectangle. (b) Aerial image of the study area (www.Norgeskart.no). The black rectangle shows the frame of Sentinel-1 sensor processed in this study.

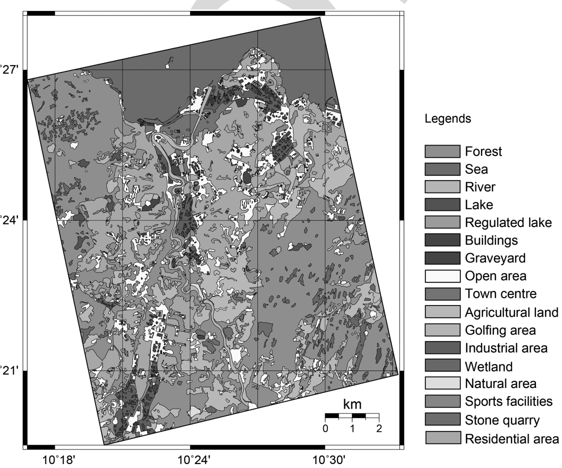

Fig. 2. Land use map of the study area (www.geonorge.no).

Trondheim city is located in central Norway. According to the Norwegian mapping authority, Kartverket, the most represented land use classes within the processed frame are vegetation, urban areas, and water bodies, covering ∼47%, ∼38%, and ∼15% of the region of interest, respectively (see Fig. 2). The urban classes mainly comprise commercial, industrial, and residential units. The commercial units, which are located in the town center, have a large (length, width, and height) and dense element of shops and service buildings. The buildings have predominantly two or more storeys with metallic constituents (having a strong reflection). Industrial regions consist of the largest buildings, developed or undeveloped, used for industrial purposes, installations for water supply, waste handling and cleaning, power plants, transformer substation, etc. In contrast to the commercial and industrial units, residential houses are smaller in size, with single- or two-storey rectangular buildings. In addition, they have been constructed mainly with wood and have tilted roofs. The buildings, for the most part, are closer than 50 m apart.

IV. Processing Strategy

Fig. 3 illustrates the flowchart of the processing developed in this paper. It includes three steps: first, preprocessing, second,

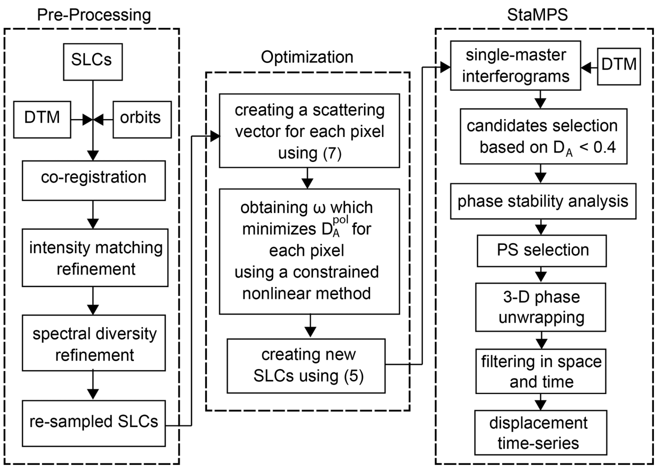

Fig. 3. Flowchart of the overall processing used in this study.

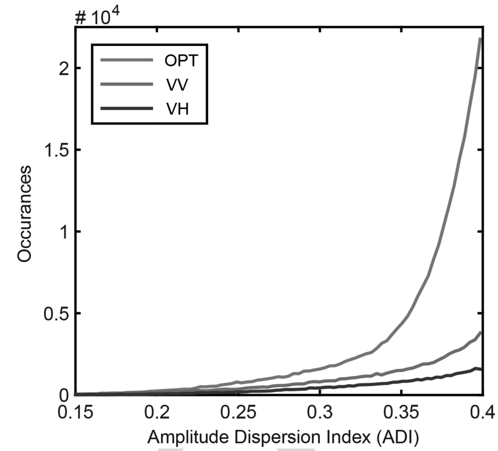

Fig. 4. Histograms of the ADI less than the considered PSC threshold (0.4) for optimum (green), VV (red), and VH (blue) channels.

optimization, and third, the PS-InSAR processing. These steps are briefly described in the following.

The scene acquired on July 25, 2015 is used as the super-master image to minimize the spatial and temporal baselines of the interferograms to be formed. The slave images are coregistered and resampled to the reference geometry (the master image) using GAMMA software [45]. In GAMMA software, the first step of the Sentinel-1 SLC co-registration procedure is based on the orbit geometry and terrain height. In the next step, the refinement of the coregistration is done iteratively using the intensity matching and the spectral diversity methods, in which the matching refinement iterates until the azimuth correction determined is better than 0.01 pixel. After reaching this quality, the spectral diversity method iterates until the azimuth correction determined is <0.0005 pixel [46].

Having made this, the precisely resampled SLCs are available. The next step is to find the projection vector that provides the minimized value of the ADI using the BFGS algorithm. Afterward, the SLCs are reproduced in optimized scattering mechanism by using (5), and the optimal interferograms are generated. To create the interferograms, we used the repeat-pass technique implemented in DORIS software [47] to be able to process further steps of the PS-InSAR analysis in StaMPS software. Initial topographic phase components are subtracted from the interferograms and, then, geocoding is done using digital terrain model at 40-m resolution provided by the Norwegian Mapping Authority.

The new differential interferograms, available after the optimization, are used as input data for the PS-InSAR algorithm in StaMPS software. The ADI threshold of 0.4 is set to identify the initial set of the PSC pixels, as thresholding on the ADI ≤ 0.4 improves computational times, reduces the data by an order of magnitude, and includes most of the PS points [48].

V. Results and Discussions

A. Dual-Polarized Versus Single-Polarized PS-InSAR

The datasets were processed using both the standard single-polarized PS-InSAR approach in StaMPS software and the described algorithm in Section IV. Fig. 4 shows the histograms of the ADI less than 0.4 (the threshold) obtained for VV, VH, and the optimum channels. As it can be seen in the figure, compared to the conventional channels, the optimum channel has significantly improved the amplitude stability. We find about 2.5 and 5.5 times as much the number of PSCs in the optimum channel as compared to that provided by single-polarized VV and VH data, respectively.

After achieving improvement in the number of candidates as a result of the optimization, phase-stability analysis was iteratively done on the identified PSCs, and the PS points were finally selected. The results from the processing of VH, VV, and optimum channels consist of approximately 37 700, 60 730, and 108 000 PS points in the processed region of interest, respectively. From the results, we find that the final number of PS points obtained by the processing of the optimum channel has been increased by approximately 186% and 78% as compared to the standard processing by VH and VV channels, respectively.

B. PS Density in Different Land Use

To illustrate the spatial patterns of the PS density-variation among the channels, the PS density obtained by the VV and VH channels have been subtracted from that, which has been obtained by the optimum channel. The results have been represented in Fig. 5(a) and (b), respectively. Clearly recognizable is that the PS density has been significantly increased across the whole processed area, but with different variations over the urban units. The maximum PS density of $\sim$2698 PS/km^2, $\sim$4427 PS/km^2, and $\sim$6942 PS/km^2, in the processed region of interest, is achieved from VH, VV, and the optimum channel, respectively.

Fig. 6 provides further insight into our findings by presenting the number of PSC and PS points detected using the conventional and optimum channels in urban and nonurban units. According to the figure, the number of PSC points in urban and nonurban units derived by the optimum channel has increased by about 3.7 and 22.9 times, respectively, as compared to the VH channel. The number of final PS points has increased by

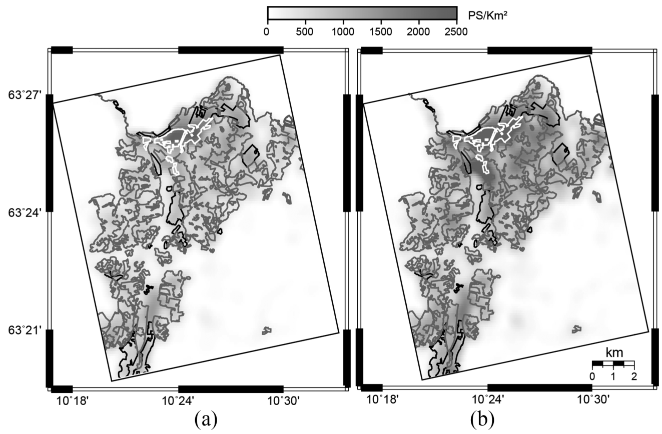

Fig. 5. Differences in the PS density between the optimum channel and (a) VV and (b) VH channels. The border of the commercial, residential, and industrial clusters have been illustrated by white, red, and black polygons, respectively.

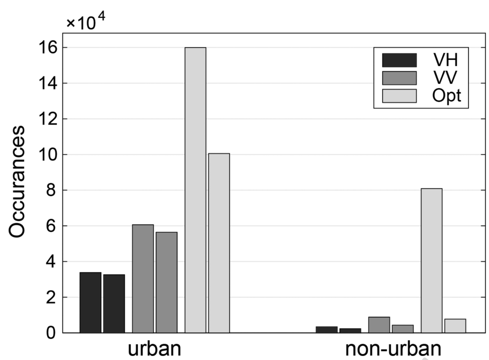

Fig. 6. Number of detected PSC (left bars) and PS (right bars) pixels detected in VH (blue), VV (green), and optimum (yellow) channels.

TABLE I
EXTRA PSC/PS PIXELS DETECTED USING THE OPTIMUM CHANNEL, AS COMPARED TO VH AND VV CHANNELS

	PSC		PS	
	VH [%]	VV [%]	VH [%]	VV [%]
urban	373	164	209	78
Non-urban	2289	818	234	79
total	547	247	186	78

about 2.1 times in urban and 2.3 times in nonurban units as compared to the VH channel. The increment in the PSC with respect to the VV channel is about 1.6 times in the urban and about 8.2 times in nonurban units. The number of final PS points in the optimum channel has increased by about 0.78 times in both units as compared to the VV channel. Table I summarizes the percentage of extra PSC and PS pixels detected using the polarimetric data in both units.

C. *Scattering Mechanism of Urban Units*

To interpret the scattering mechanism of the subsurface targets in the urban classes, we used H-alpha decomposition; the distribution of H-alpha for individual urban classes is plotted

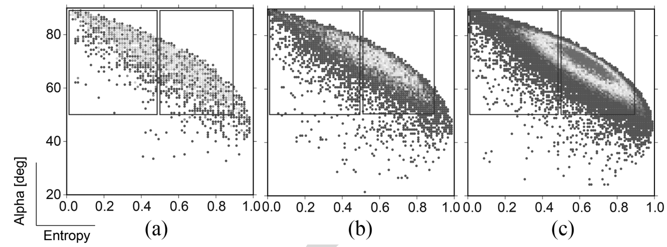

Fig. 7. H_alpha scatterplot for (a) commercial, (b) industrial, and (c) residential units, obtained from dual polarimetric decomposition of the Sentinel-1 image. The plots have been color-coded by the smoothed density of the points, in which the blue points have the minimum and the red points have the maximum density.

in Fig. 7. We empirically obtained that the scatterings with the entropy of less than 0.5 and the alpha of higher than 50° (the purple rectangle in the figure) correspond to low entropy multiple-scattering events (double-bounce scattering), such as provided by isolated dielectric and metallic dihedral scatterers. In addition, the scatterings with the entropy of 0.5–0.9 and the alpha of higher than 50° (the green rectangle in the figure) correspond to medium entropy multiple scattering, such as building and forested regions. Q2

From Fig. 7, it can be seen that in the commercial unit, the number of double-bounce scatterers are dominant. From the commercial unit to the residential unit, the distributions become more concentrated at the medium entropy. In other words, the number of double-bounce scatterers reduces, whereas the number of targets with medium-entropy scattering increases.

Over the urban units, the density in the residential areas (the red polygons in Fig. 5) has been increased, on average, from $\sim 780\,\mathrm{PS/\,km^2}$ in VV and $\sim 420\,\mathrm{PS/\,km^2}$ in VH to $\sim 1410\,\mathrm{PS/\,km^2}$ in the optimum channel. In the industrial units (the black polygons in Fig. 5), the density has been risen, on average, from $\sim 1090\,\mathrm{PS/\,km^2}$ in VV and $\sim 700\,\mathrm{PS/\,km^2}$ in VH to $\sim 1940\,\mathrm{PS/\,km^2}$ in the optimum channel. For the commercial areas (depicted by white polygons in Fig. 5), it has been increased, on average, from $\sim 2710\,\mathrm{PS/\,km^2}$ in VV and $\sim 1710\,\mathrm{PS/\,km^2}$ in VH to $\sim 4550\,\mathrm{PS/\,km^2}$ in the optimum channel. The highest density is achieved in commercial areas, which contain mostly double-bounce targets [see Fig. 7(a)], whereas the lowest density is obtained in residential areas, which contain mainly scatterers with medium entropy [see Fig. 7(c)]. Comparing the increment in densities shows that best improvement (an increase of about 80% and 235% compared to VV and VH, respectively) is achieved in residential areas, while the least increment (an increase of about 68% and 166% compared to VV and VH, respectively) is obtained in commercial areas.

D. *Comparison Between the Scattering Angles*

Comparing the optimum scattering mechanism derived from the optimization approach [see Fig. 8(a)] with the dominant scattering mechanism derived from the H-alpha decomposition [see Fig. 8(b)] shows that there is almost similar pattern between them, especially in areas, which have low entropy [see Fig. 8(c)]. To investigate the correlation between the scattering mechanisms, we extracted for each PS point, i.e., the optimum

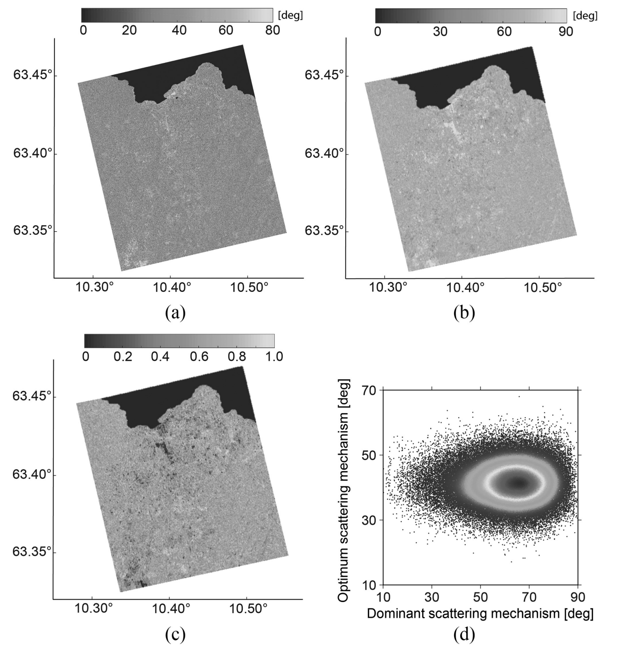

Fig. 8. (a) Optimum scattering mechanism (alpha) derived from the ADI optimization approach. (b) Dominant scattering mechanisms. (c) Entropy derived from the H-alpha decomposition. (d) Scatterplot of (a) versus (b) at the location of the PS points, color-coded by the smoothed density of the points in which blue to red color shows the lowest and the highest densities.

scattering mechanism and the dominant scattering mechanism values inside a circle with 20 m radius centered at the location of each PS point, and plotted the values in Fig. 8(d). It can be seen that, generally, the optimum alpha derived by the ADI optimization approach took lower values than the dominant alpha. The dominant alpha ranges between 10° and 90°, whereas the optimum alpha varies between 20° and 60°. However, the majority of points are concentrated in the dominant alpha values of 55°–75° and the optimum alpha values of 35°–45°, expressing that there is a good correlation in the areas with double-bounce scatterers.

Part of the differences might be caused by the fact that the ADI is computed for single-look data, so the optimum alpha derived by the ADI optimization approach is more sensitive to polarimetric features inside the resolution cell. Since the alpha derived from the decomposition is computed over a spatial window, it is defined by the averaged features of an extended area [23].

E. PSC Versus PS

In most part of the processed area, the magnitude of the VH channel is less than half of the magnitude of the VV channel. It even reaches to less than 0.1 in areas with double-bounce scattering targets. They may even degrade due to noise, and their dispersion may increase because of the existence of the different level of noise in each acquisition. As a result, the classical PS-InSAR analysis, which relies on targets with low-amplitude dispersion, is limited to select the pixels with low amplitude. Our results show that, using the optimization process, we can handle this problem and incorporate information that exist in VH in the time-series analysis, which otherwise will be lost due to the low amplitude in VH. Consequently, the number of PSC points as well as the number and density of PS points increase noticeably.

However, comparing the number of PSs with PSCs in urban areas shows a reduction of about 4%, 7%, and 37% of the candidates derived by VH, VV, and optimum channels, respectively, after phase-stability analysis. For nonurban areas, the reduction is about 32% in VH, 50% in VV, and 90% in the optimum channel. Therefore, using the optimization process, we can benefit from the VH channel despite of its low amplitude, and increase the number of PSC. However, after applying the phase-stability analysis, many of them are dropped (will be discussed in Section V-F). It is concluded that the amplitude dispersion analysis criterion alone is not sufficient for PS selection, and the phase analysis should be performed to better estimate the phase stability of the PSC points.

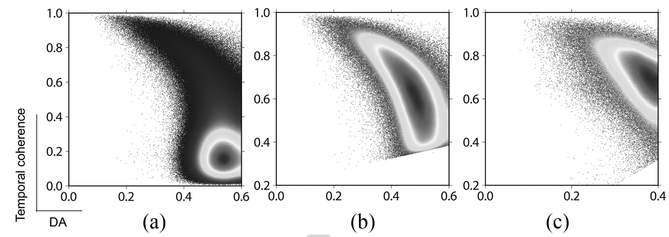

Fig. 9. Scatterplot of the distribution of the ADI versus the temporal coherence of the (a) PSC and (b) final PS points obtained by the ADI threshold of 0.6 on the VV channel, and (c) final PS points obtained by the optimum channel. The plots are color-coded by the smoothed density of the points in which blue to red color shows the lowest and the highest densities.

F. ADI Thresholding

Another way to increase the number of PS points is taking a less-constraining ADI threshold for initial selection. We considered thresholding on ADI ≤ 0.6 on the VV channel, without optimization, and compared the result with that obtained by the optimization method. Fig. 9(a) shows the distribution of the ADI versus the temporal coherence of the PS candidates, color-coded by the smoothed density of the points in which blue to red color shows the lowest and highest densities. As it can be seen in the figure, the majority of points have the ADI between 0.4 and 0.6, and the temporal coherence of less than 0.4. Fig. 9(b) shows the same scatterplot for the final PS points. It shows that most of the final PS points have the ADI between 0.4 and 0.55 and the temporal coherence of 0.4–0.8. Using this approach, 86.5% of the PSC points are discarded after the phase analysis.

In Fig. 9(c), we plotted the same distribution for the final PS points obtained by the optimum channel. Most of the final PS points have the ADI of 0.3–0.4 and the temporal coherence of 0.6–0.8. Comparing the two plots shows that, using optimization method, the final PS points have better coherence. Looking at the position of the final PS points selected by increasing the ADI threshold shows that, several points have been selected over the forest areas, which may affect the reliability of phase unwrapping.

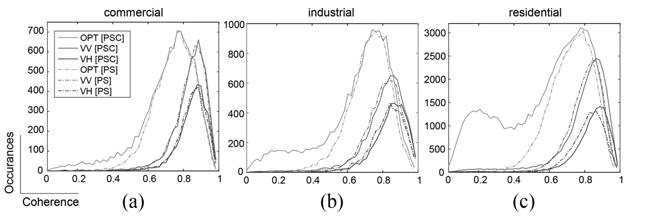

Fig. 10. Histograms of the temporal coherence values of the PSC (solid curves) and PS (dashed curves) points for optimum (green), VV (red), and VH (blue) channels in the commercial, industrial, and residential units.

G. Temporal Coherence

Fig. 10 shows the histograms of the temporal coherence values of the PSC (solid curves) and PS (dashed curves) points for the different urban units derived by the optimum (green), VV (red) and VH (blue) channels. From commercial to residential, as the number of targets with double-bounce scattering decreases, the distribution is inclined toward the double-peaks distribution. Further investigations showed that the PSCs in the left part of the distributions in industrial and residential areas are associated with pixels having high ADI (0.3–0.4), which have been selected by candidates more likely from vegetation areas. However, they have been discarded after the phase-stability analysis due to low-temporal coherence.

Comparing the distribution of the optimum and VV channels shows that the width of the distributions has increased with this method. However, the mode values changed from approximately 0.85 to 0.75, as compared to the conventional channel distributions. In addition, on the one hand, the method increases the number of PS points having the coherence of less than $\sim$0.85, but on the other hand, decreases the coherence for the points, which have the coherence of more than $\sim$0.85 in the VV channel. We clearly see that the decrease has been amplified in commercial areas and reduced in residential areas. In other words, the lessening of the high-temporal coherence values has been adversely affected by the targets type.

H. Consistency of Results

To assess the consistency between the PS-InSAR results obtained from the optimum, VV, and VH channels, it is necessary to derive the displacement rates at the same locations for the datasets. For this purpose, we extracted the rates inside a circle with 150 m radius, centered at the location of the PS pixels in the VH result, which has the lowest density among the results. To illustrate the correlations between the results, we plotted with positions given by the line of sight (LOS) displacement rate derived by the VV and VH channels, and color corresponding to the LOS rate derived by the optimum channel [see Fig. 11(a)]. The figure shows that the results are in general agreement with each other. The correlation coefficients of 0.85 and 0.92 were observed between the optimum results and VH and VV results, respectively, indicating the general consistency of the results.

As a result of the PS-InSAR processing, the LOS time-series displacement is acquired for each PS points. For comparison of the displacements in time, we plotted the mean LOS results with the associated standard deviations for PS points within a circle with 50 m radius centered at the area with maximum LOS displacement rate [see Fig. 11(b)]. The figure, in general, indicates a good agreement between the results. Some discrepancies with maximum value of 5 mm can be seen between the optimum result and two other results. However, the differences are less than their associated standard deviations. This might be caused by different PS densities, which fall into the defined circle.

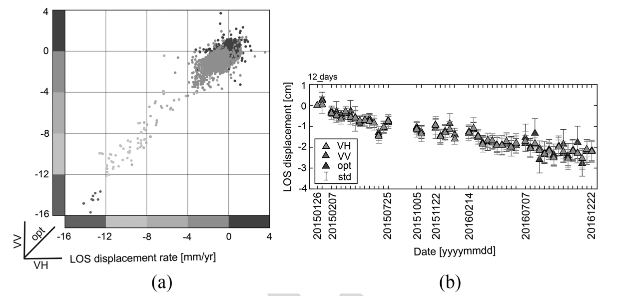

Fig. 11. (a) Scatterplot of the LOS rate derived by the VV channel against the VH channel. The color of PS points corresponds to the LOS rate derived by the optimum channel. (b) Time-series displacement of one PS point in the LOS direction is obtained by VH, VV, and optimum channels, represented by green, red, and blue triangles, respectively, with their associated standard deviations.

VI. Conclusion

We implemented a polarimetric optimization approach on Sentinel-1 dual-polarization (VV–VH) images to improve the PS-InSAR method. In general, the amplitude of the VH channel is one order of magnitude smaller than that of the VV channel. However, using the optimization method, we can incorporate the information that exists in the VH channel into the time-series analysis, which otherwise is lost due to its low amplitude. As a result of this approach, we achieved the general increment of about 78% and 186% in the number of PS points, with respect to the VV and VH channels, respectively. Further analysis on the efficiency of the method across urban units revealed that the improvement in the areas with double-bounce scatterers is less than other scatterers. In addition, the method decreases the temporal-coherence values of PS points (PS points with the coherence values of higher than 0.85) in areas with double-bounce scattering targets. We also analyzed the correlation between the LOS displacement rates and the time-series obtained by the optimum and the conventional channels, and found high correlations between them, which indicates the general consistency of the results.

Acknowledgment

The land use map and the digital terrain model have been provided by the Norwegian Mapping Authority.

References

[1] M. Esmaeili and M. Motagh, “Improved persistent scatterer analysis using amplitude dispersion index optimization of dual polarimetry data,” *ISPRS J. Photogrammetry Remote Sens.*, vol. 117, pp. 108–114, 2016.

[2] C. Colesanti, A. Ferretti, F. Novali, C. Prati, and F. Rocca, “SAR monitoring of progressive and seasonal ground deformation using the permanent scatterers technique,” *IEEE Trans. Geosci. Remote Sens.*, vol. 41, no. 7, pp. 1685–1701, Aug. 2003.

[3] M. Crosetto, E. Biescas, J. Duro, J. Closa, and A. Arnaud, "Generation of advanced ERS and Envisat interferometric SAR products using the stable point network technique," *Photogramm. Eng. Remote Sens.*, vol. 74, no. 4, pp. 443–450, 2008.

[4] A. Ferretti, C. Prati, and F. Rocca, "Nonlinear subsidence rate estimation using permanent scatterers in differential SAR interferometry," *IEEE Trans. Geosci. Remote Sens.*, vol. 38, no. 5, pp. 2202–2212, Sep. 2000.

[5] A. Ferretti, C. Prati, and F. Rocca, "Permanent scatterers in SAR interferometry," *IEEE Trans. Geosci. Remote Sens.*, vol. 39, no. 1, pp. 8–20, Jan. 2001.

[6] A. Hooper, H. Zebker, P. Segall, and B. Kampes, "A new method for measuring deformation on volcanoes and other natural terrains using InSAR persistent scatterers," *Geophys. Res. Lett.*, vol. 31, no. 23, 2004, Art. no. L23611.

[7] B. M. Kampes and R. F. Hanssen, "Ambiguity resolution for permanent scatterer interferometry," *IEEE Trans. Geosci. Remote Sens.*, vol. 42, no. 11, pp. 2446–2453, Nov. 2004.

[8] O. Mora, J. J. Mallorqui, and A. Broquetas, "Linear and nonlinear terrain deformation maps from a reduced set of interferometric SAR images," *IEEE Trans. Geosci. Remote Sens.*, vol. 41, no. 10, pp. 2243–2253, Oct. 2003.

[9] F. Cigna, R. Lasaponara, N. Masini, P. Milillo, and D. Tapete, "Persistent scatterer interferometry processing of COSMO-SkyMed StripMap HIMAGE time series to depict deformation of the historic centre of Rome, Italy," *Remote Sens.*, vol. 6, no. 12, pp. 12593–12618, 2014.

[10] P. Teatini, G. Gambolati, M. Ferronato, A. T. Settari, and D. Walters, "Land uplift due to subsurface fluid injection," *J. Geodynamics*, vol. 51, no. 1, pp. 1–16, 2011.

[11] C. Meisina *et al.*, "Geological interpretation of PSInSAR data at regional scale," *Sensors*, vol. 8, no. 11, pp. 7469–7492, 2008.

[12] V. Tofani, F. Raspini, F. Catani, and N. Casagli, "Persistent scatterer interferometry (PSI) technique for landslide characterization and monitoring," *Remote Sens.*, vol. 5, no. 3, pp. 1045–1065, 2013.

[13] R. Bürgmann, G. Hilley, A. Ferretti, and F. Novali, "Resolving vertical tectonics in the San Francisco bay area from permanent scatterer InSAR and GPS analysis," *Geology*, vol. 34, no. 3, pp. 221–224, 2006.

[14] E. Lagios *et al.*, "Combined seismicity pattern analysis, DGPS and PSInSAR studies in the broader area of Cephalonia (Greece)," *Tectonophysics*, vol. 524, pp. 43–58, 2012.

[15] M. Motagh, J. Hoffmann, B. Kampes, M. Baes, and J. Zschau, "Strain accumulation across the Gazikoy–Saros segment of the North Anatolian fault inferred from persistent scatterer interferometry and GPS measurements," *Earth Planet. Sci. Lett.*, vol. 255, no. 3, pp. 432–444, 2007.

[16] A. Peltier *et al.,* "PSInSAR as a new tool to monitor pre-eruptive volcano ground deformation: Validation using GPS measurements on Piton de la Fournaise," *Geophys. Res. Lett.*, vol. 37, no. 12, 2010, Art. no. L12301.

[17] P. Berardino, G. Fornaro, R. Lanari, and E. Sansosti, "A new algorithm for surface deformation monitoring based on small baseline differential SAR interferograms," *IEEE Trans. Geosci. Remote Sens.*, vol. 40, no. 11, pp. 2375–2383, Nov. 2002.

[18] S. R. Cloude and K. P. Papathanassiou, "Polarimetric SAR interferometry," *IEEE Trans. Geosci. Remote Sens.*, vol. 36, no. 5, pp. 1551–1565, Sep. 1998.

[19] E. Colin, C. Titin-Schnaider, and W. Tabbara, "An interferometric coherence optimization method in radar polarimetry for high-resolution imagery," *IEEE Trans. Geosci. Remote Sens.*, vol. 44, no. 1, pp. 167–175, Jan. 2006.

[20] A. G. Mullissa, V. Tolpekin, A. Stein, and D. Perissin, "Polarimetric differential SAR interferometry in an arid natural environment," *Int. J. Appl. Earth Observation Geoinformation*, vol. 59, pp. 9–18, 2017.

[21] M. Neumann, L. Ferro-Famil, and A. Reigber, "Multibaseline polarimetric SAR interferometry coherence optimization," *IEEE Geosci. Remote Sens. Lett*., vol. 5, no. 1, pp. 93–97, Jan. 2008.

[22] R. Iglesias *et al.,* "Phase quality optimization in polarimetric differential SAR interferometry," *IEEE Trans. Geosci. Remote Sens.*, vol. 52, no. 5, pp. 2875–2888, May 2014.

[23] V. D. Navarro-Sanchez and J. M. Lopez-Sanchez, "Improvement of persistent-scatterer interferometry performance by means of a polarimetric optimization," *IEEE Geosci. Remote Sens. Lett.*, vol. 9, no. 4, pp. 609–613, Jul. 2012.

[24] L. Pipia *et al.*, "Polarimetric differential SAR interferometry: First results with ground-based measurements," *IEEE Geosci. Remote Sens. Lett.*, vol. 6, no. 1, pp. 167–171, Jan. 2009.

[25] V. D. Navarro-Sanchez, J. M. Lopez-Sanchez, and L. Ferro-Famil, "Polarimetric approaches for persistent scatterers interferometry," *IEEE Trans. Geosci. Remote Sens.*, vol. 52, no. 3, pp. 1667–1676, Mar. 2014.

[26] B. Wu, L. Tong, Y. Chen, and L. He, "New methods in multibaseline polarimetric SAR interferometry coherence optimization," *IEEE Geosci. Remote Sens. Lett.*, vol. 12, no. 10, pp. 2016–2020, Oct. 2015.

[27] R. Iglesias *et al.,* "Polarimetric optimization of temporal sublook coherence for DInSAR applications," *IEEE Geosci. Remote Sens. Lett.*, vol. 12, no. 1, pp. 87–91, Jan. 2015.

[28] D. Monells, J. Mallorqui, G. Centolanza, and C. Lopez-Martinez, "Application of polarimetric techniques in DInSAR processing for space borne subsidence monitoring," in *Proc. Sci. Appl. SAR Polarimetry Polarimetric Interferometry*, 2011, vol. 695. Q3

[29] K. Ishitsuka, T. Matsuoka, and M. Tamura, "Persistent scatterer selection incorporating polarimetric SAR interferograms based on maximum likelihood theory," *IEEE Trans. Geosci. Remote Sens.*, vol. 55, no. 1, pp. 38–50, Jan. 2017.

[30] S. Samsonov and K. Tiampo, "Polarization phase difference analysis for selection of persistent scatterers in SAR interferometry," *IEEE Geosci. Remote Sens. Lett.*, vol. 8, no. 2, pp. 331–335, Mar. 2011.

[31] S. Alipour, K. F. Tiampo, S. V. Samsonov, and P. J. González, "Short-term surface deformation on the Northern Hayward fault, CA, and nearby landslides using polarimetric SAR interferometry (PolInSAR)," *Pure Appl. Geophys.*, vol. 172, no. 8, pp. 2179–2193, 2015.

[32] M. Esmaeili, M. Motagh, and A. Hooper, "Application of dual-polarimetry SAR images in multitemporal InSAR processing," *IEEE Geosci. Remote Sens. Lett.*, vol. 14, no. 9, pp. 1489–1493, Sep. 2017.

[33] V. D. Navarro-Sanchez and J. M. Lopez-Sanchez, "Spatial adaptive speckle filtering driven by temporal polarimetric statistics and its application to PSI," *IEEE Trans. Geosci. Remote Sens.*, vol. 52, no. 8, pp. 4548–4557, Aug. 2014.

[34] R. M. Goldstein and C. L. Werner, "Radar interferogram filtering for geophysical applications," *Geophys. Res. Lett.*, vol. 25, no. 21, pp. 4035–4038, 1998.

[35] A. Hooper, P. Segall, and H. Zebker, "Persistent scatterer interferometric synthetic aperture radar for crustal deformation analysis, with application to Volcán Alcedo, Galápagos," *J. Geophys. Res., Solid Earth*, vol. 112, no. B7, 2007, Art. no. B07407.

[36] A. Hooper and H. A. Zebker, "Phase unwrapping in three dimensions with application to InSAR time series," *J. Opt. Soc. Amer. A*, vol. 24, no. 9, pp. 2737–2747, 2007.

[37] S. Cloude and K. Papathanassiou, "Polarimetric optimisation in radar interferometry," *Electron. Lett.*, vol. 33, no. 13, pp. 1176–1178, 1997.

[38] K. Ji and Y. Wu, "Scattering mechanism extraction by a modified Cloude-Pottier decomposition for dual polarization SAR," *Remote Sens.*, vol. 7, no. 6, pp. 7447–7470, 2015.

[39] A. G. Mullissa, D. Perissin, V. A. Tolpekin, and A. Stein, "Polarimetry-based distributed scatterer processing method for PSI applications," *IEEE Trans. Geosci. Remote Sens.*, vol. 56, no. 6, pp. 3371–3382, Jun. 2018.

[40] V. D. Navarro-Sanchez, J. M. Lopez-Sanchez, and F. Vicente-Guijalba, "A contribution of polarimetry to satellite differential SAR interferometry: Increasing the number of pixel candidates," *IEEE Geosci. Remote Sens. Lett.*, vol. 7, no. 2, pp. 276–280, Apr. 2010.

[41] R. Battiti and F. Masulli, "BFGS optimization for faster and automated supervised learning," in *Proc. Int. Neural Netw. Conf.*, Springer, 1990, pp. 757–760.

[42] S. R. Cloude and E. Pottier, "A review of target decomposition theorems in radar polarimetry," *IEEE Trans. Geosci. Remote Sens.*, vol. 34, no. 2, pp. 498–518, Mar. 1996.

[43] S. R. Cloude and E. Pottier, "An entropy based classification scheme for land applications of polarimetric SAR," *IEEE Trans. Geosci. Remote Sensing*, vol. 35, no. 1, pp. 68–78, Jan. 1997.

[44] S. Cloude, "The dual polarization entropy/alpha decomposition: A PALSAR case study," in *Proc. Sci. Appl. SAR Polarimetry Polarimetric Interferometry*, 2007, vol. 644.

[45] U. Wegmüller and C. Werner, "Gamma SAR processor and interferometry software," in *Proc. 3rd ERS Symp.*, 1997, pp. 1687–1692.

[46] R. Scheiber and A. Moreira, "Coregistration of interferometric SAR images using spectral diversity," *IEEE Trans. Geosci. Remote Sens.*, vol. 38, no. 5, pp. 2179–2191, Sep. 2000.

[47] B. M. Kampes, R. F. Hanssen, and Z. Perski, "Radar interferometry with public domain tools," in *Proc. FRINGE*, 2003, vol. 3.

[48] A. J. Hooper, "Persistent scatter radar interferometry for crustal deformation studies and modeling of volcanic deformation," Ph.D. dissertations, Stanford Univ., Sanford, CA, USA, 2006. Q4

Authors' photographs and biographies not available at the time of publication.

GENERAL INSTRUCTIONS

- Authors: When accessing and uploading your corrections at the Author Gateway, please note we cannot accept new source files as corrections for your paper. Do not send new Latex, Word, or PDF files, as we cannot simply "overwrite" your paper. Please submit your corrections as an annotated PDF or as clearly written list of corrections, with location in paper. You can also upload revised graphics to the Gateway.
- Authors: Please note that once you click "approve with no changes," the proofing process is now complete and your paper will be sent for final publication and printing. Once your paper is posted on Xplore, it is considered final and the article of record. No further changes will be allowed at this point so please ensure scrutiny of your final proof.
- Authors: Unless invited or otherwise informed, a mandatory Excessive Paper Length charge of $200.00 per page (beginning with page 7 and beyond) is required for papers in excess of six (6) printed pages for JSTARS. If you have any questions regarding overlength page charges, need an invoice, or have any other billing questions, please contact reprints@ieee.org as they handle these billing requests.

QUERIES

Q1. Author: Please confirm or add details for any funding or financial support for the research of this article.
Q2. Author: Please check whether the edits made in the sentence "To interpret the scattering mechanism of the subsurface . . . " retain the intended sense.
Q3. Author: Please provide page numbers for [28], [44], and [47].
Q4. Author: Please provide name of the department in Ref. [48].